Supporting Information for:

Title: Liquid spherical shells are a non-equilibrium steady state

Authors: Alexander M. Bergmann,[1*] Jonathan Bauermann,[2,3*] Giacomo Bartolucci,[2,3*] Carsten Donau,[1*] Michele Stasi,[1] Anna-Lena Holtmannspötter,[1] Frank Jülicher,[2,3] Christoph A. Weber,[4,+] Job Boekhoven[1,+]

Affiliations:
[1]School of Natural Sciences, Department of Chemistry, Technical University of Munich, Lichtenbergstrasse 4, 85748 Garching, Germany.

[2]Max Planck Institute for the Physics of Complex Systems, Nöthnitzer Strasse 38, 01187 Dresden, Germany.

[3]Center for Systems Biology Dresden, Pfotenhauerstrasse 108, 01307 Dresden, Germany.

[4]Faculty of Mathematics, Natural Sciences, and Materials Engineering: Institute of Physics, University of Augsburg, Universitätsstrasse 1, 86159 Augsburg, Germany.

*equal contribution

+corresponding author

Table of Contents

I.   Supplementary Methods

I. Supplementary Methods

(A) Determination of rate constants of the chemical reaction cycle. The concentration profiles of the precursor and its corresponding anhydride (product) were determined by HPLC, whereas NMR quantified fuel and waste.
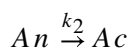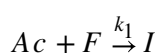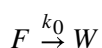
Due to the instability of the product, a quenching technique was used with an amine that converts the product into a quantifiable amide[1-3]. To a solution (145 µL) of 10 mM precursor in 200 mM MES at pH 5.3 was added a solution (5 µL) of 5-20 mM DIC in acetonitrile in an HPLC vial. After each time point, 10 µL of the reaction mixture was added to 20 µL of an aqueous solution of ethylamine (400 mM). The resulting clear solution was then injected into the HPLC, and the concentration of the precursor and product was calculated from the resulting peak integrals.

Quantification of fuel and waste: 5-20 mM DIC was added to a solution (1 mL) of 200 mM MES at pH 5.3 and vortexed for 30 s to dissolve all DIC. The sample also contained 10 vol% D_2O and 80 mM acetonitrile (ACN) as a reference. 10 mM precursor was added to 500 µl of this solution. The solution was vortexed and added to an NMR tube. ^{1}H-NMR measurements were performed on a 300 MHz NMR every 5 min until no more DIC was detected. The concentrations of fuel and waste were then calculated from the peak integrals, which were compared with the acetonitrile reference. The chemical shifts of the compared signals were ^{1}H NMR (300 MHz, D_2O): ACN δ (ppm) = 2.07 (s, 3H, CH3), DIC δ (ppm) = 1.22-1.23 (d, 12H, CH3), DIU δ (ppm) = 1.09-1.10 (d, 12H, CH3).

The obtained data from the HPLC and NMR experiments were then fitted via a kinetic model in python.

(B) Kinetic model.

The reaction cycle in a homogeneous system is described in a kinetic modeled according to the following mechanism:

$$F \xrightarrow{k_0} W$$

$$Ac + F \xrightarrow{k_1} I$$

$$I \xrightarrow{k_{An}} An + W$$

$$I \xrightarrow{k_{Ac}} Ac + W$$

$$An \xrightarrow{k_2} Ac$$

Ac is the dicarboxylic acid, F is the fuel, I is the intermediate O-acylurea, W is the waste, and An is the anhydride.

The mechanism translates into the following set of differential equations:

$$
\begin{cases}
\frac{d[Ac]}{dt} = -k_1 \cdot [Ac] \cdot [F] + k_2 \cdot [An] + k_{Ac} \cdot [I] \\
\frac{d[F]}{dt} = -k_1 \cdot [Ac] \cdot [F] - k_0 \cdot [F] \\
\frac{d[W]}{dT} = +k_0 \cdot [F] + k_{Ac} \cdot [I] + k_{An} \cdot [I] \\
\frac{d[An]}{dt} = +k_{An} \cdot [I] - k_2 \cdot [An] \\
\frac{d[I]}{dt} = +k_1 \cdot [Ac] \cdot [F] - k_{An} \cdot [I] - k_{Ac} \cdot [I]
\end{cases}
\qquad (1)
$$

We then applied steady-state approximation to obtain:

$$
\frac{d[I]}{dt} = +k_1 \cdot [Ac] \cdot [F] - k_{An} \cdot [I] - k_{Ac} \cdot [I] \approx 0 \Rightarrow [I] \approx \frac{k_1 \cdot [Ac] \cdot [F]}{k_{An} \cdot \left(\frac{k_{Ac}}{k_{An}} + 1\right)}
$$

We called $\frac{k_{Ac}}{k_{An}} = K$ and used the relation above in the set of differential equations to obtain:

$$
\begin{cases}
\frac{d[Ac]}{dt} = -k_1 \cdot [Ac] \cdot [F] + k_2 \cdot [An] + \frac{K \cdot k_1 \cdot [Ac] \cdot [F]}{(K+1)} \\
\frac{d[F]}{dt} = -k_1 \cdot [Ac] \cdot [F] - k_0 \cdot [F] \\
\frac{d[W]}{dT} = +k_0 \cdot [F] + k_1 \cdot [Ac] \cdot [F] \\
\frac{d[An]}{dt} = +\frac{k_1 \cdot [Ac] \cdot [F]}{(K+1)} - k_2 \cdot [An]
\end{cases}
\qquad (2)
$$

Experimental data were fit to the equation system (2) using a custom program in Python 3 (kinmodel, https://github.com/scotthartley/kinmodel) previously published by the group of Hartley and applied to similar systems[4]. To calculate concentrations of precursor and product under continuous fueling, the change in fuel concentration was set to 0 ($\frac{d[F]}{dt}$=0).

(C) Determination of the partitioning and concentration of molecules inside and outside of the droplet phase. To determine the amount of precursor, product*, and fuel in the dilute phase and inside passive droplets for the phase diagram, we measured their concentrations using HPLC, fluorescence spectroscopy, and NMR.

For the precursor, we quantified the fraction of the precursor that remained in the dilute phase of passive droplets by HPLC. 5 mM pSS was added to a solution containing 10-x mM precursor and x mM product* (total peptide concentration = 10 mM) or 20 mM precursor (without product*) in 200 mM MES at pH 5.3. The turbid suspension (V = 150 μL) was vortexed, incubated for 5 min, and then centrifuged for another 15 min at 20,412×g. 100 μL of the supernatant was removed and added into an HPLC inlet. 1 μL of NaCl (4 M) aqueous solution was added to dissolve residual turbidity. The resulting clear solution was injected into the HPLC and compared to a solution containing 10-x mM precursor or 20 mM precursor

without pSS to calculate the fraction of precursor that remained in the supernatant after droplet formation.

Product*: we quantified the fraction of product* as a measure for the anhydride product that remained in the dilute phase of passive droplets by fluorescence spectroscopy because its concentration in the supernatant could not be determined accurately via HPLC (peak overlap with the precursor, low fraction remaining in supernatant). Therefore, we used NBD-G(RG)$_3$N-NH$_2$ (fluorescent analog of product*), which partitions similarly into the droplet phase as product*[5]. To a solution of 10-x mM precursor and x mM product* (total peptide concentration = 10 mM) or 2 mM product* (without precursor) in 200 mM MES at pH 5.3 with 1 µM NBD-G(RG)$_3$N-NH$_2$ were added 5 mM pSS. The turbid suspension (V = 150 µL) was vortexed, incubated for 5 min, and then centrifuged for another 15 min at 20,412×g. 100 µL of the supernatant was removed and added into an Eppendorf tube. 1 µL of an aqueous solution of NaCl (4 M) was added to dissolve residual turbidity. The fluorescence of the sample was then measured on the fluorimeter (Excitation at 467 nm, emission at 526 nm). To account for the dependence of the fluorescence of dyes on their environment[6], we prepared an identical sample without NBD-G(RG)$_3$N-NH$_2$. We added the supernatant (96 µL) to an Eppendorf tube containing 1 µL of an aqueous solution of NaCl (4 M). To the clear solution, we then added 1 µM NBD-G(RG)$_3$N-NH$_2$ (4 µL) as in the previous sample and measured its fluorescence intensity. The intensity ratio between these two samples was used as the fraction of the fluorescent molecules that remained in the supernatant.

Fuel: we quantified the fraction of fuel partitioned into the droplet phase of passive droplets using NMR. To avoid the reaction of precursor and fuel, passive droplets consisting only of product* and pSS were used. 10 mM DIC (1.55 µl) was added to a solution (1 mL) containing 2 mM product* and 5 mM pSS in 200 mM MES at pH 5.3. The solution was vortexed and incubated for 5 min. The sample was centrifuged for 5 min at 20,412×g and the supernatant was carefully removed. The residual coacervate phase (about 1 µL) was dissolved in a solution (50 µL) containing 400 mM NaCl, 560 mM borate buffer at pH 10, 80 mM ACN as standard, and 20 vol% D$_2$O. The high pH prevents further hydrolysis of DIC between sample preparation and measurement. the DIC concentration was determined by ^{1}H-NMR spectroscopy. Blank measurements without droplets were performed to account for residual DIC containing dilute phase on the walls of the sample containers after the removal of the supernatant. As a blank, 10 mM DIC was added to a solution (1 mL) containing 200 mM MES at pH 5.3. The blank solution without droplets was treated similarly to the solution with droplets. The sample was centrifuged for 5 min at 20,412×g and the supernatant was carefully removed. A solution (50 µL) containing 400 mM NaCl, 560 mM borate buffer at pH 10, 80 mM ACN as standard, and 20 vol% D$_2$O was added and the DIC concentration was determined by ^{1}H-NMR spectroscopy. The concentrations of fuel were then calculated from the peak

integrals which were compared with the acetonitrile reference and corrected by the blank. The chemical shifts of the compared signals were ^{1}H NMR (500 MHz, D_2O): ACN δ (ppm) = 2.07 (s, 3H, CH3), DIC δ (ppm) = 1.22-1.23 (d, 12H, CH3).

Combined with the total volumes of the droplet pellets (see method below), we calculated the partitioning of the individual molecules in passive droplets (Table S1-3). The resulting error bars of the concentration inside the droplets (c_{in}) and the partitioning coefficient (K) represent the accumulated standard deviation from the experiments measuring the fraction of molecules in the supernatant (c_{out}) and the total volumes of the coacervate pellets.

(D) Determination of total droplet volumes. To calculate the partitioning of the precursor, product*, and fuel in the droplet phase for the phase diagram, the total droplet volume was estimated via a centrifugation assay. For that, samples (200 µL) of passive droplets containing 10-x mM precursor and x mM product* (total peptide concentration = 10 mM), 20 mM precursor (without product), or 2 mM product* (without precursor) in 200 mM MES at pH 5.3 with 15 µM sulforhodamine B (for visualization) were prepared. After the addition of 5 mM pSS, the turbid suspensions were incubated for 5 min and then centrifuged for another 15 min at 20,412×g. The volume of the droplet pellets (0.4-2 µL) was then compared to size standards visually (Table S1-3).

(E) Estimating the concentration of product and fuel in the microreactors. To validate whether the continuously fueled microreactors contain a steady-state level of product and fuel, we chose an indirect quantification method by HPLC for the product, and quantification by NMR for the fuel. We assumed that the diffusion of fuel from the surrounding oil phase into a microfluidic reactor (r= 5-50 µm) is fast and should be comparable to a two-phase system in a glass vial under vigorous stirring. We used perfluorinated oil without surfactant in these experiments to avoid stabilized emulsions.

Product: 250 µL of an aqueous solution containing 10 mM precursor in 200 mM MES at pH 5.3 was added on top of perfluorinated oil (Novec 7500, 1 mL) in an HPLC vial. We started the reaction network by the addition of 0.5 M DIC into the oil phase and vigorously stirring the reaction mixture. To determine the concentration of the product, 10 µL of the aqueous phase was quenched with 20 µL of an aqueous solution of ethylamine (400 mM) every 30 min. The reaction between the amine and the product yields a stable amide that can be quantified[1,2]. We correlated the resulting peak integrals of the amide to the product assuming that the absorption of the amide is equal to the absorption of the precursor (Fig. S1).

Fuel and waste in the steady state: 1.25 mL of 10 mM precursor in 200 mM MES at pH 5.3 were added to 5 mL of perfluorinated oil (Novec 7500) containing 0.5 M DIC. The mixture was vigorously stirred and samples of 25 µL were taken and quenched with 25 µL 640 mM borate

buffer at pH 10 with 20 vol% D_2O and 80 mM acetonitrile as a reference. The high pH inhibits the direct DIC hydration and the reaction of the precursor with DIC to ensure that the time until the sample is measured is not influencing the measured concentrations of fuel and waste. Samples are measured by ^{1}H-NMR spectroscopy. The concentrations of fuel and waste were then calculated from the peak integrals which were compared to the acetonitrile peak reference (Fig. S1). The chemical shifts of the compared signals were ^{1}H NMR (400 MHz, D_2O): ACN δ (ppm) = 2.07 (s, 3H, CH3), DIC δ (ppm) = 1.22-1.23 (d, 12H, CH3), DIU δ (ppm) = 1.09-1.10 (d, 12H, CH3).

Variation of the fuel concentration in the microreactor: The concentration of fuel in the aqueous phase was measured for different fuel concentrations in the oil phase to determine the partitioning into the aqueous phase. 1 mL of 200 mM MES at pH 5.3 is added to 10 mL of perfluorinated oil (Novec 7500) containing 0.25 – 1.0 M DIC. The mixtures were vortexed for 20 s and after the phases have separated 250 µl of the aqueous phase are added to 250 µl of 640 mM borate buffer at pH 10 with 20 vol% D_2O and 80 mM acetonitrile as a reference. Samples were measured by ^{1}H-NMR spectroscopy. The concentrations of fuel were then calculated from the peak integrals which were compared to the acetonitrile peak reference (Fig. S4D). The chemical shifts of the compared signals were ^{1}H NMR (400 MHz, D_2O): ACN δ (ppm) = 2.07 (s, 3H, CH3), DIC δ (ppm) = 1.22-1.23 (d, 12H, CH3).

(F) Thermodynamic model for the experimental phase diagram

In the theoretical model, we use an effective ternary mixture where the influence of fuel, waste, and polyanion is accounted for in an implicit manner; details see section (P). The effective components of the ternary mixture are solvent, the precursor A, and the product B. For these components, equilibrium concentrations inside and outside were determined experimentally; see Table (1-2). To fit the corresponding experimental diagram, we use a Flory-Huggins free energy density given as [7,8]

$$f(c_A, c_B) = k_B T \left[\sum_{i=A,B,S} c_i \log(r_i c_i) + \sum_{ij=AB,AS,BS} \chi_{ij} \, r_i c_i \, r_j c_j \right] , \qquad (3)$$

where c_A and c_B denote the the concentrations of components A and B, respectively. In Eq. (3), we have combined the molecular volumes ν_A, ν_B, and ν_S in the ratios introduced the molecular volume ratios $r_i = \nu_i/\nu_S$. The concentration of the solvent follows from the incompressibility of the mixture, $c_S = 1/\nu_S - r_A c_A - r_B c_B$. This free energy density depends on five parameters: the molecular volume rations, r_A and r_B, and the interaction parameters, χ_{AB}, χ_{AS}, and χ_{AB}. We determine these five parameters by fitting experimental measurements of different phase equilibria. At phase equilibria, the chemical potentials $\mu_i = \partial f/\partial c_i$ of components A and B and the osmotic pressure $\Pi = -f + \sum_{i=A,B} c_i \mu_i$ are balanced between the phases. For the measurements, the product was stabilised against hydrolysis by mutating the C terminal aspartic acid for an asparagine. This chemical modification yields a peptide that has the same interaction propensities as the product but is stable, i.e., it does not convert to the precursor. Every measured point in the phase diagram gives three constraints

$$\mu_A\left(c_A^{I}, c_B^{I}\right) = \mu_A\left(c_A^{II}, c_B^{II}\right), \qquad (4)$$

$$\mu_B\left(c_A^{I}, c_B^{I}\right) = \mu_B\left(c_A^{II}, c_B^{II}\right), \qquad (5)$$

$$\Pi\left(c_A^{I}, c_B^{I}\right) = \Pi\left(c_A^{II}, c_B^{II}\right). \qquad (6)$$

We obtained the five unknown parameters by simultaneously minimizing the deviations for the

resulting 13 conditions. The best fit was obtained for $r_A = 35.1$, $r_B = 19.4$, $\chi_{AB} = -0.18$, $\chi_{AS} = 0.78$, and $\chi_{AS} = 1.29$. In Ext. Data Fig. 9, we show the corresponding phase diagram together with the experimental measured concentration values. The last thermodynamic parameter needed for our model is the surface tension γ. Since γ is difficult to estimate within our experimental setup, we use the value $\gamma = 75\,\mu\text{N m}^{-1}$ which is thousand times smaller than the air-water interfacial tension. Our value is in good agreement with surface tensions measured for similar coacervates [9]. Note that the used value is slightly larger than for biological condensates [10].

**(G) Sharp interface model for the kinetics of active droplets and active spherical shells**

In general, diffusion is driven by spatial gradients of chemical potentials, while reactions minimize the difference in chemical potentials between products and reactants. For the following, we consider linearized kinetic equations, where diffusion is driven by spatial gradients of concentrations and the reaction

$$A \rightleftharpoons B \,, \tag{7}$$

is driven by the differences in concentrations of the respective components. The resulting kinetic parameters in terms of diffusivities and rate coefficients are then determined via experimental measurements, see experimental section. Therefore, the dynamical equation for c_A and c_B read [11,12]

$$\partial_t c_i^\alpha = D_i^\alpha \nabla^2 c_i^\alpha + k_i^\alpha c_j^\alpha - k_{ji}^\alpha c_i^\alpha \,. \tag{8}$$

In the case of spherical active droplets, there are two different domains with $\alpha = \text{I,II}$, where I denotes the dense phase of droplet and II denotes the dilute phase outside the droplet. For spherical symmetric active spherical shells, three different domains exist, $\alpha = \text{I,II,III}$, where I denotes the dilute phase within the core of the spherical shell, III labels the dense phase of the spherical shell, and II correspond to the dilute phase outside the spherical shell.
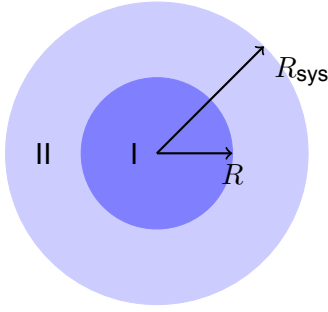
Sketch I. Geometry for active droplet.

(P1) Chemically active droplet

We calculate the radial symmetric stationary profiles that solve Eq. (8) in the two different domains as a function of the radial coordinate r. At the droplet's core ($r = 0$), we impose no flux boundary conditions for the solution of domain I. Similarly, no flux boundary conditions are imposed at system boundary $r = R_{sys}$ for the solution in domain II. The two domains are coupled at the sharp interface at position $r = R$. Here, we impose concentration boundary conditions $c_A^\alpha(R) = a^\alpha$, $c_B^\alpha(R) = b^\alpha$. These concentrations are later determined self-consistently. For these boundary conditions, the stationary solutions for domain I read

$$c_A^I(r) = \frac{b^I - a^I \rho_k^I}{\rho_D^I - \rho_k^I} \frac{R \sinh(r/\lambda^I)}{r \sinh(R/\lambda^I)} + \frac{a^I \rho_D^I - b^I}{\rho_D^I - \rho_k^I}, \tag{9}$$

$$c_B^I(r) = \rho_D^I \frac{b^I - a^I \rho_k}{\rho_D^I - \rho_k^I} \frac{R \sinh(r/\lambda^I)}{r \sinh(R/\lambda^I)} + \rho_k^I \frac{a^I \rho_D^I - b^I}{\rho_D^I - \rho_k^I}, \tag{10}$$

while in domain II, the stationary solutions follow

$$c_A^{II}(r) = \frac{a^{II} k_{BA}^{II} - b^{II} k_{AB}}{k_{BA}^{II} - k_{AB}^{II} \rho_D^{II}} \frac{R}{r} \frac{\sinh(r/\lambda^{II}) + \Phi \cosh(r/\lambda^{II})}{\sinh(R/\lambda^{II}) + \Phi \cosh(R/\lambda^{II})} - \frac{a^{II} k_{BA}^{II} - b^{II} k_{AB} \rho_D^{II}}{k_{BA}^{II} - k_{AB}^{II} \rho_D^{II}}, \tag{11}$$

$$c_B^{II}(r) = \rho_D^{II} \frac{a^{II} k_{BA}^{II} - b^{II} k_{AB}}{k_{BA}^{II} - k_{AB}^{II} \rho_D^{II}} \frac{R}{r} \frac{\sinh(r/\lambda^{II}) + \Phi \cosh(r/\lambda^{II})}{\sinh(R/\lambda^{II}) + \Phi \cosh(R/\lambda^{II})} - \rho_k^{II} \frac{a^{II} k_{BA}^{II} - b^{II} k_{AB} \rho_D^{II}}{k_{BA}^{II} - k_{AB}^{II} \rho_D^{II}}. \tag{12}$$

We have made use of $\lambda^\alpha = \sqrt{D_A^\alpha D_B^\alpha / (D_A^\alpha k_{AB}^\alpha + D_B^\alpha k_{BA}^\alpha)}$, $\rho_D^\alpha = -D_A^\alpha / D_B^\alpha$, and $\rho_k^\alpha = k_{BA}^\alpha / k_{AB}^\alpha$, where $\alpha = I, II$ indicate the phases.

The coefficient $\Phi = -(\lambda^{II} R_{sys} \cosh[\lambda^{II} R_{sys}] - \sinh[\lambda^{II} R_{sys}]) / (\lambda^{II} R_{sys} \sinh[\lambda^{II} R_{sys}] - \cosh[\lambda^{II} R_{sys}])$ ensures the zero flux boundary condition at the system radius.

Finally, we have to determine the four interface concentrations a^I, a^{II}, b^I, b^{II} and the position of the interface R. For this, we need five constraints. Three of these constraints follow from the

assumption of a local equilibrium of phase separation [12]

$$\mu_A(a^I, b^I) = \mu_A(a^{II}, b^{II}), \tag{13}$$

$$\mu_B(a^I, b^I) = \mu_B(a^{II}, b^{II}), \tag{14}$$

$$\Pi(a^I, b^I) = \Pi(a^{II}, b^{II}) - \frac{2\gamma}{R}. \tag{15}$$

Furthermore, the total of A and B have to be conserved in the system,

$$V_{\text{sys}}\, \bar{c}_{\text{tot}} = \frac{4}{3}\pi \left[(a^I + b^I)R^3 + (a^{II} + b^{II})(R_{\text{sys}}^3 - R^3) \right], \tag{16}$$

where $c_{\text{tot}} = c_A + c_B$ is the conserved quantity associated to the chemical reaction in Eq. (7). Finally, the conservation law at the interface in the stationary state requires

$$j_i^I(R) = j_i^{II}(R), \tag{17}$$

where $j_i^\alpha = -D_i^\alpha \partial_r c_i^\alpha$ is radial component of the material flux density. Note that the stationary solution implies that $j_A^\alpha(r) = -j_B^\alpha(r)$. Thus, the constraint Eq. (17) is fulfilled simultaneously for both components A and B, making the total number of independent constraints equal to five.
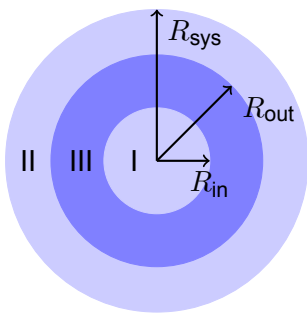
Sketch II. Geometry for active spherical shell.

(P2) Chemically active spherical shell

In the spherical shell state, the stationary concentration profiles in domain I and II have the same functional form as in the active droplet state. In addition, there is the shell domain III between domain I and domain II. Here, the stationary solutions of Eq. (8), with concentration boundary conditions on the interfaces left and right

$$c_A^{\text{III}}(r) = K_1 \frac{\sinh\left(r/\lambda^{\text{III}}\right)}{r} + K_2 \frac{\cosh\left(r/\lambda^{\text{III}}\right)}{r} + K_3 + \frac{K_4}{r}, \tag{18}$$

$$c_B^{\text{III}}(r) = \rho_D^{\text{III}} \left[K_1 \frac{\sinh\left(r/\lambda^{\text{III}}\right)}{r} + K_2 \frac{\cosh\left(r/\lambda^{\text{III}}\right)}{r} \right] + \rho_k^{\text{III}} \left[K_3 + \frac{K_4}{r} \right]. \tag{19}$$

Here, we have abbreviated

$$K_1 = \frac{\text{csch}[(R_{\text{out}} - R_{\text{in}})/\lambda^{\text{III}}]}{K_{BA}^{\text{III}} - \rho_D^{\text{III}} K_{AB}^{\text{III}}} \left[(b^{\text{III,in}} K_{AB}^{\text{III}} - a^{\text{III,in}} K_{BA}^{\text{III}}) R_{\text{in}} \cosh\left(R_{\text{out}}/\lambda^{\text{III}}\right) \right.$$
$$\left. - (b^{\text{III,out}} K_{AB}^{\text{III}} - a^{\text{III,out}} K_{BA}^{\text{III}}) R_{\text{out}} \cosh\left(R_{\text{in}}/\lambda^{\text{III}}\right) \right], \tag{20}$$

$$K_2 = \frac{\text{csch}[(R_{\text{out}} - R_{\text{in}})/\lambda^{\text{III}}]}{K_{BA}^{\text{III}} - \rho_D^{\text{III}} K_{AB}^{\text{III}}} \left[(b^{\text{III,out}} K_{AB}^{\text{III}} - a^{\text{III,out}} K_{BA}^{\text{III}}) R_{\text{out}} \sinh\left(R_{\text{in}}/\lambda^{\text{III}}\right) \right.$$
$$\left. - (b^{\text{III,in}} K_{AB}^{\text{III}} - a^{\text{III,in}} K_{BA}^{\text{III}}) R_{\text{in}} \sinh\left(R_{\text{out}}/\lambda^{\text{III}}\right) \right], \tag{21}$$

$$K_3 = \frac{(a^{\text{III,out}} D_A^{\text{III}} + b^{\text{III,out}} D_B^{\text{III}}) R_{\text{out}} - (a^{\text{III,in}} D_A^{\text{III}} + b^{\text{III,in}} D_B^{\text{III}}) R_{\text{in}}}{(D_A^{\text{III}} + D_B^{\text{III}} \rho_k^{\text{III}})(R_{\text{out}} - R_{\text{in}})}, \tag{22}$$

$$K_4 = \frac{(a^{\text{III,in}} - a^{\text{III,out}}) D_A^{\text{III}} + (b^{\text{III,in}} - b^{\text{III,out}}) D_B^{\text{III}}}{(D_A^{\text{III}} + D_B^{\text{III}} \rho_k^{\text{III}})(R_{\text{out}} - R_{\text{in}})} R_{\text{in}} R_{\text{out}}. \tag{23}$$

We introduced $\lambda^{\text{III}} = \sqrt{D_A^{\text{III}} D_B^{\text{III}}/(D_A^{\text{III}} k_{AB}^{\text{III}} + D_B^{\text{III}} k_{BA}^{\text{III}})}$, $\rho_D^{\text{III}} = -D_A^{\text{III}}/D_B^{\text{III}}$, and $\rho_k^{\text{III}} = k_{BA}^{\text{III}}/k_{AB}^{\text{III}}$, in analogy to phases I and II.

Finally, we have to determine the eight interface concentrations a^{I}, $a^{\text{III,in}}$, $a^{\text{III,out}}$, a^{II}, b^{I}, $b^{\text{III,in}}$, $b^{\text{III,out}}$, and b^{II}, and the two positions of the interfaces R_{in} and R_{out}. For this, we need ten constraints, three of which follow from the assumption of a local equilibrium of phase separation at R_{in}

$$\mu_A(a^{\text{I}}, b^{\text{I}}) = \mu_A(a^{\text{III,in}}, b^{\text{III,in}}), \tag{24}$$

$$\mu_B(a^{\text{I}}, b^{\text{I}}) = \mu_B(a^{\text{III,in}}, b^{\text{III,in}}), \tag{25}$$

$$\Pi(a^{\text{I}}, b^{\text{I}}) = \Pi(a^{\text{III,in}}, b^{\text{III,in}}) - \frac{2\gamma}{R_{\text{in}}}, \tag{26}$$

and three from local equilibrium of phase separation at R_{out}

$$\mu_A(a^{\text{III,out}}, b^{\text{III,out}}) = \mu_A(a^{\text{II}}, b^{\text{II}}) \,, \tag{27}$$

$$\mu_B(a^{\text{III,out}}, b^{\text{III,out}}) = \mu_B(a^{\text{II}}, b^{\text{II}}) \,, \tag{28}$$

$$\Pi(a^{\text{III,out}}, b^{\text{III,out}}) = \Pi(a^{\text{II}}, b^{\text{II}}) - \frac{2\gamma}{R_{\text{out}}} \,. \tag{29}$$

These six equations must be supplemented with a global conservation law

$$\bar{c}_{\text{tot}} \, V_{\text{sys}} = \int dV \, (c_A + c_B) \,, \tag{30}$$

a local conservation law at R_{in},

$$j_i^{\text{I}}(R_{\text{in}}) = j_i^{\text{II}}(R_{\text{in}}) \,, \tag{31}$$

and a local conservation law at R_{out},

$$j_i^{\text{II}}(R_{\text{out}}) = j_i^{\text{III}}(R_{\text{out}}) \,. \tag{32}$$

In contrast to domains I and II, in domain III, $j_A \neq -j_B$, due to the $1/r$ term in the solution of the Laplace equation. Thus, the two flux equations have to be balanced for the components A and B at one interface, respectively. Due to the symmetry of the stationary solutions, one equality is automatically fulfilled at the second interface. Thus, we are left with three independent constraints coming from the local conservation laws at the interfaces Eqs. (31) and (32).

(H) Parameter values used in numerical calculations

If not indicated otherwise, we chose the parameters indicated in Table 6 for the numerical calculations. For the figures shown in this work, we fixed the following parameter values as stated in Table 7. To illustrate the dependency of the stationary profiles on the parameters, we show the concentration profiles in composition space for different settings of the ratio of $D_A^{\text{II}}/D_B^{\text{II}}$, the surface tension γ, and the ratio of the activation rates $k_{BA}^{\text{I}}/k_{BA}^{\text{II}}$ in Sup. Fig. 1.

(I) Calculations of free energies and free energy rates

We can estimate the free energy difference between a spherical shell stationary state and the corresponding homogeneous state with the same average concentrations

$$\bar{c}_i = \frac{1}{V_{\text{sys}}} \int dV \, c_i \,, \tag{33}$$

with $i = A, B$. In the following estimates, we will consider spherical shells at steady state corresponding to $R_{\text{sys}} = 35 \, \mu$m. We start from the concentrations in the coexisting phases, c_i^+ and c_i^-, corresponding to the spherical shell average concentration $\bar{c}_i$. Neglecting the interface contribution and considering each phase homogeneous, the free energy in the spherical shell state can be estimated directly via

$$F_{\text{mix}} = V^+ f^+ + (V_{\text{sys}} - V^-)f^- \,, \tag{34}$$

where the free energy density in each phase is $f^\pm = f(c_A^\pm, c_B^\pm)$ and V^+ is the total volume of the dense phase. With the parameters displayed in Table 6, this difference yields $F_{\text{mix}} = 2$ nJ.

This free energy can be compared with the total activation free energy, defined as the energy of a B molecule times the number of excess B molecules at the spherical shell steady state

$$F_{\text{act}} = \Delta\omega(\bar{c}_B - c_B^0)V_{\text{sys}} \,, \tag{35}$$

where $c_B^0 = c_{\text{tot}}/[1 + \exp(\Delta\Omega)]$ is the B concentration in the homogeneous equilibrium state, i.e., without fuel present, and $\Delta\Omega$ is the activation free energy of a single A molecule, which is roughly $10 \, k_B T$ [13] As outlined in the main text, making use of the parameters in Table 6, we estimate $F_{\text{act}} \simeq 80$ nJ.

Next, we estimate the number of particles that constantly get converted from the precursor

A into the product B, per unit time and volume,

$$n_{\text{tot}} = \frac{1}{V_{\text{sys}}} \int dV \, c_A \, k_{BA} \,, \tag{36}$$

which determines the total free energy turned over per time and volume

$$J_{\text{tot}} = \Delta\Omega \, n_{\text{tot}} \,. \tag{37}$$

Here, $\Delta\Omega$ denotes the activation energy supplied by fuel to the precursor to form a product. Using the parameters shown in Table 6, $c_{\mathsf{F}} = 8.6$ mM, and $\Delta\Omega \simeq 10 k_B T$, we obtain $n_{\text{tot}} = 4 \cdot 10^6 \, \text{s}^{-1} \mu\text{m}^{-1}$ and $J_{\text{tot}} = 0.25$ W/L as outlined in the main text.

We can also estimate the free energy flux through the spherical shell interface. Specifically, we calculate the flux of product B through the interface where each product is activated by $\Delta\Omega$

$$J_{\text{int}} = \left[4\pi R_{\text{out}}^2 \, j_A^{\text{II}}(R_{\text{out}}) - 4\pi R_{\text{in}}^2 \, j_A^{\text{I}}(R_{\text{in}}) \right] \Delta\omega / V_{\text{sys}} \,. \tag{38}$$

Using the parameters shown in Table 6, and $\Delta\omega \sim 10 \, k_B T$, this leads to an energy influx per unit time of $J_{\text{int}} = 0.198$ W/L. Comparing it to the total power J_{tot}, this leads to an efficiency $J_{\text{int}}/J_{\text{tot}}$ around 70%. In Sup. Fig. 2, we explored how J_{tot} and J_{shell} vary upon changes in the activation rate, induced by changes of the fuel concentration. Note that in our minimal model, the fuel enters implicitly in the activation rate. As expected, J_{tot}, which represents the total power needed to activate precursor A to product B to their respective values at the non-equilibrium steady state (see definition in Eq. (37)), varies linearly with the fuel concentration. On the other hand, the free energy transported to the spherical shell interface, J_{int}, scales sublinearly with fuel concentration. This is because the higher the fuel the more activation occurs inside, making the B particle flux at the interface less pronounced. As a consequence, the efficiency decreases as fuel concentration increases.

II. Supplementary Text

Supplementary discussion 1. We quantified the interaction strength between the peptides (precursor and product) with pSS by means of ITC. We used Ac-F(RG)$_3$N-NH$_2$ (product*) as a measure for the product (anhydride of precursor) since both molecules are structurally very similar and contain the same positive net charge[5].

Supplementary discussion 2. For the mechanism evaluation, we wanted to quantify the precursor, product and fuel partitioning in the active droplets. However, for the setup of continuously fueled droplets, a centrifugation assay is not directly possible. Determining the partitioning of the molecules in droplets fueled with a batch of fuel is possible for a specific time point with a centrifugation assay. Still, the molecular composition of the dilute and the dense phase is time-dependent (with respect to fuel addition) and thus this data cannot be used to build a phase diagram. Furthermore, a proceeding of the reactions cannot be prevented during the preparation of these assays. To avoid this time dependence, we prepared passive droplets containing only one of the reactive components at a time. For the precursor and the product, passive droplets at different ratios of precursor and product* (without fuel) were used to measure active droplets in a steady state. To determine the partitioning of the fuel, we prepared droplets consisting only of product* and pSS (no precursor) which were therefore passive as well.

III. Supplementary tables

Total concentrations			Precursor			
Precursor [mM]	Product* [mM]	pSS [mM]	c_{in} [mM]	c_{out} [mM]	V_{coa}/V_{dilute} [vol%]	$K_{partitioning}$ [c_{in}/c_{out}]
20	0	5	309 ± 323	18.2 ± 1.5 (91%)	0.57 ± 0.10	17 ± 19
9.5	0.5	5	782 ± 584	7.8 ± 0.9 (82%)	0.22 ± 0.04	101 ± 88
9	1	5	734 ± 229	6.1 ± 0.5 (67%)	0.40 ± 0.05	121 ± 49
8	2	5	655 ± 236	6.2 ± 0.3 (78%)	0.28 ± 0.05	106 ± 43
0	2	5	-	-	-	-

Table S1: *Experimentally determined values for the partitioning of the precursor in passive droplets for the phase diagram.*

Total concentrations			Product*			
Precursor [mM]	Product* [mM]	pSS [mM]	c_{in} [mM]	c_{out} [mM]	V_{coa}/V_{dilute} [vol%]	$K_{partitioning}$ [c_{in}/c_{out}]
20	0	5	-	-	-	-
9.5	0.5	5	176 ± 48	0.11 ± 0.03 (23%)	0.22 ± 0.04	1545 ± 904
9	1	5	233 ± 35	0.07 ± 0.02 (7%)	0.40 ± 0.05	3360 ± 1645
8	2	5	692 ± 139	0.10 ± 0.0 (5%)	0.28 ± 0.05	7146 ± 3258
0	2	5	699 ± 434	0.78 ± 0.08 (39%)	0.18 ± 0.05	901 ± 653

Table S2: *Experimentally determined values for the partitioning of the product* in passive droplets for the phase diagram.*

Total concentrations			Fuel			
Precursor [mM]	Product* [mM]	pSS [mM]	c_{in} [mM]	c_{out} [mM]	V_{coa}/V_{dilute} [vol%]	$K_{partitioning}$ [c_{in}/c_{out}]
0	2	5	14.4 ± 17.3	9.98 (99.8%)	0.10 ± 0.01	1.44 ± 1.73

Table S3: *Experimentally determined values for the partitioning of the fuel in passive droplets.*

Diffusivity	Spherical shell	Droplet
$D_{precursor}$ [μm^2/s]	0.060 ± 0.010	0.042 ± 0.003
$D_{product*}$ [μm^2/s]	0.029 ± 0.008	0.032 ± 0.003

Table S4: *Experimentally determined values for the diffusivities in the active droplet and the active spherical shell.*

reaction constant	Value
k_0	$2.9 \cdot 10^{-4}$ s^{-1}
k_1	$1.7 \pm 0.08 \cdot 10^{-1}$ M^{-1} s^{-1}
K	1.34 ± 1.0
k_2	$1.2 \pm 0.9 \cdot 10^{-2}$ s^{-1}

Table S5: *Kinetic parameters determined by the kinetic model.*

Quantity	Symbol	Value	Reference
Interaction parameter precursor - product	χ_{AB}	-0.18	SI (F)
Interaction parameter precursor - solvent	χ_{AS}	0.78	SI (F)
Interaction parameter product - solvent	χ_{BS}	1.28	SI (F)
Precursor relative molecular volume	r_A	35.1	SI (F)
Product relative molecular volume	r_B	19.4	SI (F)
Surface tension	γ	$75\,\mu\mathrm{N\ m^{-1}}$	SI (F)
Activation rate outside the drop	k_{BA}^{II}	$0.17\,c_\mathrm{F}\ \mathrm{M^{-1}s^{-1}}$	SI (B) and Tab.5
Activation rate inside the drop	k_{BA}^{I}	$0.51\,c_\mathrm{F}\ \mathrm{M^{-1}s^{-1}}$	SI (B) and Tab.5
Deactivation rate outside the drop	k_{AB}^{II}	$0.012\ \mathrm{s^{-1}}$	SI (B) and Tab.5
Deactivation rate inside the drop	k_{AB}^{I}	$0.012\ \mathrm{s^{-1}}$	SI (B) and Tab.5
Diffusion coefficient of A outside the drop	D_A^{II}	$300\ \mu\mathrm{m^2\ s^{-1}}$	14
Diffusion coefficient of B outside the drop	D_B^{II}	$300\ \mu\mathrm{m^2\ s^{-1}}$	14
Diffusion coefficient of A inside the drop	D_A^{I}	$0.04\ \mu\mathrm{m^2\ s^{-1}}$	Tab.4
Diffusion coefficient of B inside the drop	D_B^{I}	$0.0073\ \mu\mathrm{m^2\ s^{-1}}$	Tab.4
Activation rate outside the spherical shell	k_{BA}^{II}	$0.17\,c_\mathrm{F}\ \mathrm{M^{-1}s^{-1}}$	SI (B) and Tab.5
Activation rate in the spherical shell shell	k_{BA}^{III}	$0.51\,c_\mathrm{F}\ \mathrm{M^{-1}s^{-1}}$	SI (B) and Tab.5
Activation rate in the spherical shell core	k_{BA}^{I}	$0.17\,c_\mathrm{F}\ \mathrm{M^{-1}s^{-1}}$	SSI (B) and Tab.5
Deactivation rate outside the spherical shell	k_{AB}^{II}	$0.012\ \mathrm{s^{-1}}$	SI (B) and Tab.5
Deactivation rate in the spherical shell shell	k_{AB}^{III}	$0.012\ \mathrm{s^{-1}}$	SI (B) and Tab.5
Deactivation rate in the spherical shell core	k_{AB}^{I}	$0.012\ \mathrm{s^{-1}}$	SI (B) and Tab.5
Diffusion coefficient of A outside the spherical shell	D_A^{II}	$300\ \mu\mathrm{m^2\ s^{-1}}$	14
Diffusion coefficient of B outside the spherical shell	D_B^{II}	$300\ \mu\mathrm{m^2\ s^{-1}}$	14
Diffusion coefficient of A in the spherical shell shell	D_A^{III}	$0.04\ \mu\mathrm{m^2\ s^{-1}}$	Tab.4
Diffusion coefficient of B inside spherical shell shell	D_B^{III}	$0.0073\ \mu\mathrm{m^2\ s^{-1}}$	Tab.4
Diffusion coefficient of A inside the spherical shell core	D_A^{I}	$300\ \mu\mathrm{m^2\ s^{-1}}$	14
Diffusion coefficient of B inside the spherical shell core	D_B^{I}	$300\ \mu\mathrm{m^2\ s^{-1}}$	14

Table S 6: Table with input parameters used in the numerical calculations.

Figure	Quantity	Symbol	Value
Fig. 4 C and D	System radius	R_sys	35 μm
Fig. 4 C and D	Fuel concentration	c_fuel	8.6 mM
Fig. 4 E	System radius	R_sys	17.5 μm
Fig. 4 E	Fuel concentration	c_fuel	8.6 mM
Fig. 4 G	System radius	R_sys	25 μm
Fig. 4 G	Fuel concentration	c_fuel	10 mM
Fig. 4 H	System radius	R_sys	25 μm
Fig. 4 H	Fuel concentration	c_fuel	10 mM
Fig. 4 H	Dif. coef. of A in inside the shell	D_A^III	as indicated by $D_\text{Precursor}$
Fig. 4 H	Dif. coef. of B in inside the shell	D_B^III	D_A^III/5.5
Ext. Data Fig. 10 A-C	System radius	R_sys	25 μm
Ext. Data Fig. 10 B, C	Fuel concentration	c_fuel	8.6 mM
Sup. Fig. 1 A-D	System radius	R_sys	20 μm
Sup. Fig. 1 B	Ratio of dif. inside the drople	$\frac{D_A^\text{II}}{D_A^\text{II}}$	$\{1, 2, 4, 5.5, 10\}$ (ind. by arrow)
Sup. Fig. 1 C	Surface tension	γ	$\{25\mu\text{N}, 75\mu\text{N}, 175\mu\text{N}\}$ (ind. by arrow)
Sup. Fig. 1 D	Ratio of act. rates	$\frac{k_\text{BA}^\text{I}}{k_\text{BA}^\text{I}}$	$\{0.1, 3, 10\}$ (ind. by arrow)
Sup. Fig. 2	System radius	R_sys	35 μm

Table S 7: Table with input parameters used for specific figures.

IV. Supplementary Figures
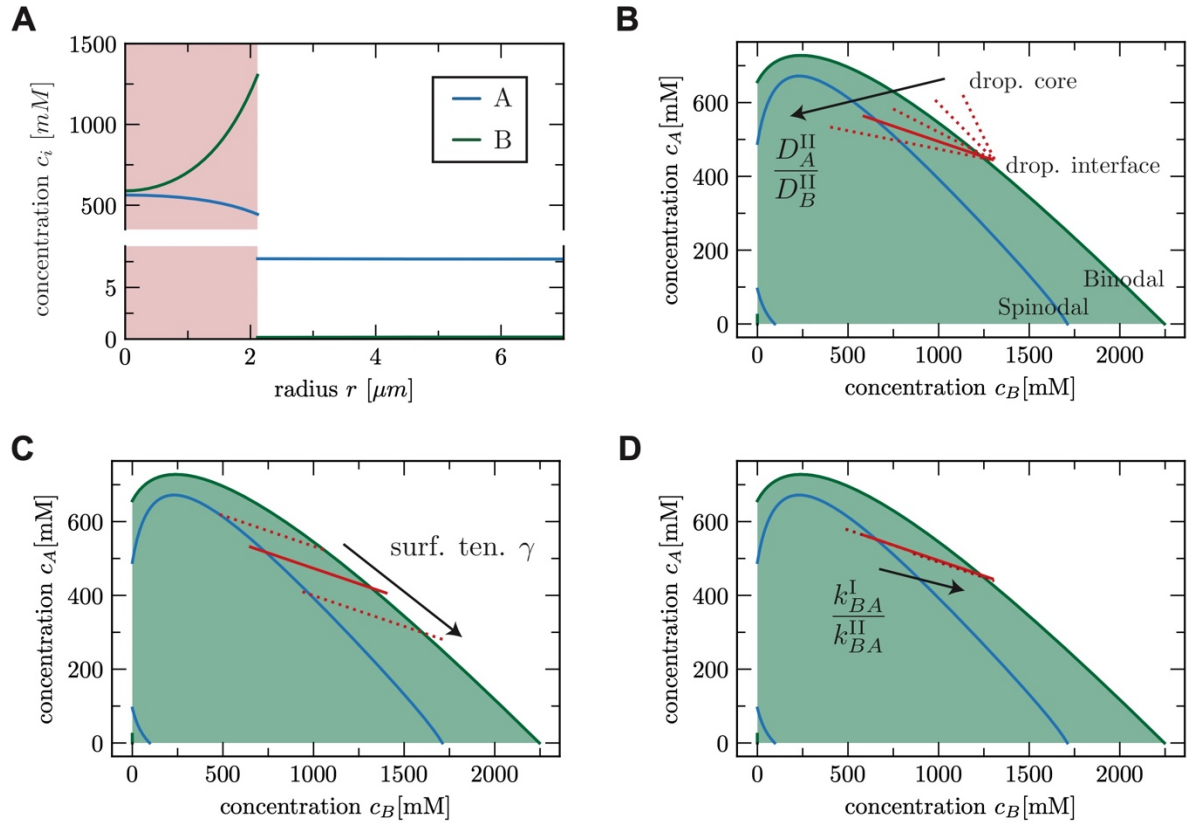
Supplementary Figure 1. Influence of different parameter choices. A Concentration values of A and B as a function of the radial distance r from the droplet center (red shaded domain is the droplet inside). **B-D** Concentration profiles of the components A and B of the droplet domain (red shaded domain in **A**) in composition space (red line) in addition to the binodal line (green) and the spinodal line (blue). Red solid line corresponds to the kinetic parameters used in the main text (Tab. 6 and 7).
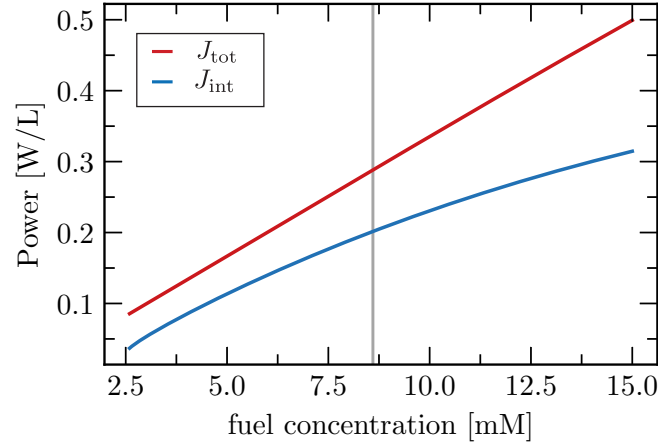
Supplementary Figure 2. Influence of fuel concentration on power turn over in the spherical shell state. *The red curve represents the power per unit volume needed to constantly activate particles from state A to B, J_{tot}. We compare it to the free energy transported through the interface corresponding to activated B particles crossing the interface, J_{int} (blue curve). The vertical line corresponds to the fuel concentration value used for the estimates in the main text. In the shown fuel concentration range, the efficiency J_{int}/J_{tot} varies non monotonically between 46% and 70%.*

V. Supplementary Movies

Supplementary movie 1. Spherical shell formation upon dissolution. *Confocal micrograph timelapse series of a solution of 22 mM precursor, 5 mM pSS in 200 mM MES at pH 5.3 with 0.1 µM sulforhodamine B as a dye and fueled with 20 mM DIC. The active droplets grew and fused initially and big droplets formed spherical shells upon dissolution. Imaging was done in PVA-coated ibidi chambers.*

Supplementary movie 2. Dissolution without spherical shell formation. *Confocal micrograph timelapse series of a solution of 22 mM precursor, 5 mM pSS in 200 mM MES at pH 5.3 with 0.1 µM sulforhodamine B as a dye and fueled with 10 mM DIC. The active droplets grew and fused initially but no spherical shells were formed upon dissolution. Imaging was done in PVA-coated ibidi chambers.*

Supplementary movie 3. Formation of a stable active droplet. *Confocal micrograph timelapse series of a solution of 10 mM precursor, 5 mM pSS in 200 mM MES at pH 5.3 with 0.1 µM sulforhodamine B as a dye. To achieve a steady state, 0.5 M DIC was added to the oil phase. The active droplets grew and fused until they reached a stable size of $r < r_{unstable}$. The time-lapse series represents the maximum z-projection of a z-stack throughout one microreactor. Imaging was started 10 min after the addition of fuel.*

Supplementary movie 4. Stable active droplet. *Confocal micrograph timelapse series of a solution of 10 mM precursor, 5 mM pSS in 200 mM MES at pH 5.3 with 0.1 µM sulforhodamine B as a dye. To achieve a steady state, 0.5 M DIC was added to the oil phase. Start of imaging was 2 h after the addition of fuel. A representative stable active droplet with $r < r_{unstable}$.*

Supplementary movie 5. Stable active shell. *Confocal micrograph timelapse series of a solution of 10 mM precursor, 5 mM pSS in 200 mM MES at pH 5.3 with 0.1 µM sulforhodamine B as a dye. To achieve a steady state, 0.5 M DIC was added to the oil phase. Start of imaging was 3 h after the addition of fuel. A representative stable active shell with $r > r_{unstable}$.*

Supplementary movie 6. Transition of an active droplet into an active spherical shell. *Confocal micrograph timelapse series of a solution of 10 mM precursor, 5 mM pSS in 200 mM MES at pH 5.3 with 0.1 µM sulforhodamine B as a dye. To achieve a steady state, 0.5 M DIC was added to the oil phase. An active droplet with a critical radius larger than $r_{unstable}$ transitioned into an active spherical shell. Imaging was done in a microreactor. Imaging was started 1 h after the addition of fuel.*

VI. Supplementary References

1   Schnitter, F. & Boekhoven, J. A Method to Quench Carbodiimide-Fueled Self-Assembly. *ChemSystemsChem* **3** (2020). https://doi.org:10.1002/syst.202000037

2   Donau, C. *et al.* Active coacervate droplets as a model for membraneless organelles and protocells. *Nature Communications* **11**, 5167 (2020). https://doi.org:10.1038/s41467-020-18815-9

3   Spath, F. *et al.* Molecular Design of Chemically Fueled Peptide-Polyelectrolyte Coacervate-Based Assemblies. *Journal of the American Chemical Society* **143**, 4782-4789 (2021). https://doi.org:10.1021/jacs.1c01148

4   Jayalath, I. M., Wang, H., Mantel, G., Kariyawasam, L. S. & Hartley, C. S. Chemically Fueled Transient Geometry Changes in Diphenic Acids. *Organic Letters* **22**, 7567-7571 (2020). https://doi.org:10.1021/acs.orglett.0c02757

5   Donau, C., Spath, F., Stasi, M., Bergmann, A. M. & Boekhoven, J. Phase Transitions in Chemically Fueled, Multiphase Complex Coacervate Droplets. *Angewandte Chemie International Edition* **61**, e202211905 (2022). https://doi.org:10.1002/anie.202211905

6   Nott, T. J. *et al.* Phase transition of a disordered nuage protein generates environmentally responsive membraneless organelles. *Mol Cell* **57**, 936-947 (2015). https://doi.org:10.1016/j.molcel.2015.01.013

7   Flory, P. J. Thermodynamics of High Polymer Solutions. *The Journal of Chemical Physics* **10**, 51-61 (1942). https://doi.org:10.1063/1.1723621

8   Huggins, M. L. Thermodynamic Properties of Solutions of Long-Chain Compounds. *Transactions of the New York Academy of Sciences* **4**, 107-107 (1942). https://doi.org:https://doi.org/10.1111/j.2164-0947.1942.tb00827.x

9   Spruijt, E., Sprakel, J., Cohen Stuart, M. A. & van der Gucht, J. Interfacial tension between a complex coacervate phase and its coexisting aqueous phase. *Soft Matter* **6**, 172-178 (2010). https://doi.org:10.1039/B911541B

10   Brangwynne, C. P. *et al.* Germline P Granules Are Liquid Droplets That Localize by Controlled Dissolution/Condensation. *Science* **324**, 1729-1732 (2009). https://doi.org:doi:10.1126/science.1172046

11   Weber, C. A., Zwicker, D., Jülicher, F. & Lee, C. F. Physics of active emulsions. *Reports on Progress in Physics* **82**, 064601 (2019). https://doi.org:10.1088/1361-6633/ab052b

12   Bauermann, J., Weber, C. A. & Jülicher, F. Energy and Matter Supply for Active Droplets. *Annalen der Physik* **534**, 2200132 (2022). https://doi.org:https://doi.org/10.1002/andp.202200132

13   Higuchi, T., Eberson, L. & McRae, J. D. Acid anhydride-free acid equilibria in water in some substituted succinic acid systems and their interaction with aniline. *Journal of the American Chemical Society* **89**, 3001-3004 (1967). https://doi.org:10.1021/ja00988a036

14   Miyamoto, S. & Shimono, K. Molecular Modeling to Estimate the Diffusion Coefficients of Drugs and Other Small Molecules. *Molecules* **25** (2020). https://doi.org:10.3390/molecules25225340